2D Materials

PAPER • **OPEN ACCESS**

Enhanced vacuum ultraviolet photoemission from graphene nanoribbons

To cite this article: Martina Corso *et al* 2024 *2D Mater.* **11** 015008

IOP Publishing 2D Mater. **11** (2024) 015008 https://doi.org/10.1088/2053-1583/ad047e

2D Materials

CrossMark

OPEN ACCESS

RECEIVED
6 March 2023

REVISED
5 October 2023

ACCEPTED FOR PUBLICATION
18 October 2023

PUBLISHED
3 November 2023

PAPER

Enhanced vacuum ultraviolet photoemission from graphene nanoribbons

Martina Corso[1,2,*], **Jorge Lobo-Checa**[3,4], **Andrew P Weber**[1,2,5], **Ignacio Piquero-Zulaica**[6], **Zakaria M Abd El-Fattah**[7], **Patrick Le Fèvre**[8], **J Enrique Ortega**[1,2,9] **and Eugene Krasovskii**[2,10,11,*]

[1] Centro de Física de Materiales CFM/MPC (CSIC-UPV/EHU), 20018 Donostia-San Sebastián, Spain
[2] Donostia International Physics Center, 20018 Donostia-San Sebastián, Spain
[3] Instituto de Nanociencia y Materiales de Aragón (INMA), CSIC-Universidad de Zaragoza, 50009 Zaragoza, Spain
[4] Departamento de Física de la Materia Condensada, Universidad de Zaragoza, 50009 Zaragoza, Spain
[5] Instituto de Ciencias Fotónicas, 08860 Barcelona, Spain
[6] Physics Department E20, Technical University of Munich (TUM), 85748 Garching, Germany
[7] Physics Department, Faculty of Science, Al-Azhar University, Nasr City, 11884 Cairo, Egypt
[8] Synchrotron SOLEIL, L'Orme des Merisiers, Départementale 128, 91190 Saint-Aubin, France
[9] Departamento de Física Aplicada I, Universidad del País Vasco, San Sebastián, Spain
[10] Departamento de Polímeros y Materiales Avanzados: Física, Química y Tecnología, Universidad del País Vasco-Euskal Herriko Unibertsitatea, 20080 Donostia-San Sebastián, Spain
[11] Ikerbasque, Basque Foundation for Science, 48013 Bilbao, Spain
[*] Authors to whom any correspondence should be addressed.

E-mail: martina.corso@csic.es and eugene.krasovskii@ehu.eus

Keywords: graphene, nanoribbons, angle-resolved photoemission, electronic structure, one-step theory

Supplementary material for this article is available online

Abstract

Photon-energy dependence of photoemission from seven-atoms-wide armchair graphene nanoribbons (GNRs) is studied experimentally and theoretically up to $\hbar\omega = 95$ eV. A strong photon energy dependence of the normal emission from the valence band maximum (VB$_1$) is observed, sharply peaked at $\hbar\omega = 12$ eV. The detailed analysis of the light-polarization dependence of the photoemission from VB$_1$ unambiguously characterizes the symmetry of the state. The experimental observations are analyzed based on *ab initio* one-step theory of photoemission. Off-normal emission is studied in detail and its relation to the standing-wave character of the valence band states is discussed. Excellent agreement with the earlier experiment (Senkovskiy *et al* 2018 *2D Mater.* **5** 035007) is obtained. Rapid variations of the intensity with the ribbon-transverse photoelectron momentum are predicted from the *ab initio* theory, which are at variance with the prediction of the tight-binding rigid-wall model. These findings can help interpret angle-resolved photoemission measurements of similar systems. Moreover, the strong enhancement of the photoyield could trigger the GNR application as narrow-band photodetectors and contribute to the design of novel photocathodes for vacuum ultraviolet photodetection.

1. Introduction

The development of high performance photocathodes is a key challenge in various technologies, such as electron injectors, particle accelerators, or photodetectors. These applications require the production of quasi-monochromatic electrons, high quantum efficiencies, and low thermal emittance to reduce noise and dark currents. Such requirements get even more demanding depending on the compatibility with the photon energy, the working environment, and the final application. In the case of ultraviolet (UV) photodetectors, largely employed in Space research, solar- and astrophysics, earth monitoring and high-resolution lithography in electronic industry, the stability under high UV irradiation and solar-blindness are often critical [1]. The most common materials used nowadays in solid-state UV detectors are semiconductors with wide band gaps above 3.1 eV (400 nm) such as diamond, Al$_x$Ga$_{1-x}$N alloys, boron nitride, and Zn compounds [2]. Those materials are far from being ideal because they lack high crystalline quality and contain many defects and impurities that create trap states, which influence the charge carrier mobility and lead to inefficiency and prolonged photoresponse times [3].

The latest searches for new materials for photodetection are focusing on ultra-thin one- and two-dimensional materials due to their strong interaction with light [4], ultra-fast charge transport [5], and electronic structure tunability. Notably, defects in graphene-related materials can be prevented by bottom–up fabrication techniques based on on-surface synthesis (OSS) reactions, which enable the growth of the desired nanostructures with atomic precision [6]. Indeed, surface guided chemical reactions of predesigned molecules in ultra-high vacuum (UHV) conditions yield graphene nanoribbons (GNRs) whose properties can be controlled and tailored at the atomic level [6–8]. These GNRs are nowadays considered a promising class of materials for electronic and optoelectronic applications because their electronic structure (semiconducting or metallic) can widely vary depending on the edge geometry (zigzag or armchair), width, and chemical functionalization [8–11]. Moreover, non-trivial topological states can be formed [12–14] or π-magnetism due to radicals can emerge [15, 16].

Chemically inert armchair type GNRs of different widths produced by OSS have been already implemented in device architectures as field effect transistors, demonstrating high potential for technological applications [9]. In particular, ordered arrays of seven carbon atoms wide armchair GNRs (7-AGNRs) were successfully implemented in photoconductive photodetectors demonstrating high responsivity, low dark current and sensitivity to incoming light polarization in the visible spectral range [17]. It is important to understand how these unique characteristics manifest themselves in the UV range. Up to now, only few studies have addressed the photoemission response of GNRs with varying photon energy and polarization [18]. In particular, the highest energy valence band (VB_1) was believed [19] to be exclusively accessible with p-polarized light at 45 eV and high emission angles, $k \sim 1.5\,\text{Å}^{-1}$. Contrarily, some of us demonstrated that such band could also be detected at normal emission using a common laboratory source with $\hbar\omega = 21$ eV [18]. This calls for a deeper understanding of photoemission from GNRs, which is essential in targeting optoelectronic applications that go beyond the visible spectral range. In [19] the angular dependence of photoemission from 7-AGNRs was interpreted in terms of quantized graphene states. Here, we revisit the validity of this approach from the point of view of an *ab initio* theory.

In this work we shed light on the photoemission properties of 7-AGNRs as a function of the photon energy and polarization. This is achieved by combining synchrotron based angle-resolved photoemission spectroscopy (ARPES) measurements on well-aligned 7-AGNRs on Au(788) with *ab initio* one-step photoemission theory. We find experimentally and corroborate theoretically a strong enhancement of photoemission at $\hbar\omega = 12$ eV for the 7-AGNRs. The spectral narrowness of the discovered feature suggests its applicability in photocathodes for vacuum UV photodetection. Based on the one-step theory, we reproduce the experiment of [19] and predict sharp angular variations of the intensity at small emission angles. We thus foresee the extensive use of GNRs in narrow-band photodetection with polarization and direction sensitivity.

2. Results and discussion

2.1. Photoemission paradigm and scattering states

We employ a rigorous, well-established, and generally applicable one-step theory of photoemission [20–24], in which the electron excitation, scattering in the nanoribbon, and transport to the detector are treated as a single process. Then the angle-dependent photocurrent $I(\omega, \mathbf{k}_{||})$ is obtained as the transition probability from the initial state $|\,\mathrm{i}\mathbf{k}_{||}\rangle$ to the time reversed LEED (low energy electron diffraction) state $|\,\mathrm{f}\mathbf{k}_{||}\rangle$:

$$I\left(\omega, \mathbf{k}_{||}\right) \sim \sqrt{E_\mathrm{f} - E_\mathrm{vac}}\,\left|\langle \mathrm{f}\mathbf{k}_{||}\,|\hat{o}|\,\mathrm{i}\mathbf{k}_{||}\rangle\right|^2, \qquad (1)$$

where $\langle \mathbf{r}\,|\,\mathrm{f}\mathbf{k}_{||}\rangle = \Phi^*_\mathrm{LEED}(\mathbf{r})$ is the time reversed LEED wave function at energy E_f and crystal momentum parallel to the ribbon $\mathbf{k}_{||}$. E_vac is the vacuum level (kinetic energy zero). The interaction with the photon field is calculated in the dipole approximation: $\hat{o} = -i\nabla \cdot \mathbf{e}$, where $\mathbf{e}$ is the direction of the electric field $\mathbf{E}$ of the light wave. The LEED wave function $\Phi_\mathrm{LEED}(\mathbf{r})$ is a scattering solution for a plane wave incident onto a free-standing grating of periodically arranged hydrogenated seven armchair nanoribbons (with the supercell lattice constant in the y direction $a = 23.3$ a.u., where 1 a.u. is the Bohr radius). Inside the nanoribbon layer Φ_LEED satisfies the Schrödinger equation $\hat{H}\Phi = E\Phi$, with the Hamiltonian $\hat{H} = -\Delta + V(\mathbf{r}) - iV_\mathrm{i}$ containing the imaginary potential $-iV_\mathrm{i}$ to allow for the inelastic scattering of the outgoing electron. Because here the interaction with the electronic system is limited to the monolayer, the absorbing potential V_i is set to zero outside a thin slab between $z = -1$ and 1 a.u. (see figure 1) and inside the slab it is $V_\mathrm{i} = 1$ eV. The absorbing potential smooths the constant initial state (CIS) spectra $I(\omega)$ and reduces the peak intensities without affecting the overall shape of the curves.

In the LEED calculation the electron is incident from the right, and the left vacuum half-space $z < z_\mathrm{L}$ contains the transmitted plane waves, see figure 1 (the presence of the substrate is not taken into account). In the scattering region $z_\mathrm{L} \leqslant z \leqslant z_\mathrm{R}$ an all-electron representation of $\Phi_\mathrm{LEED}(\mathbf{r})$ is obtained in terms of

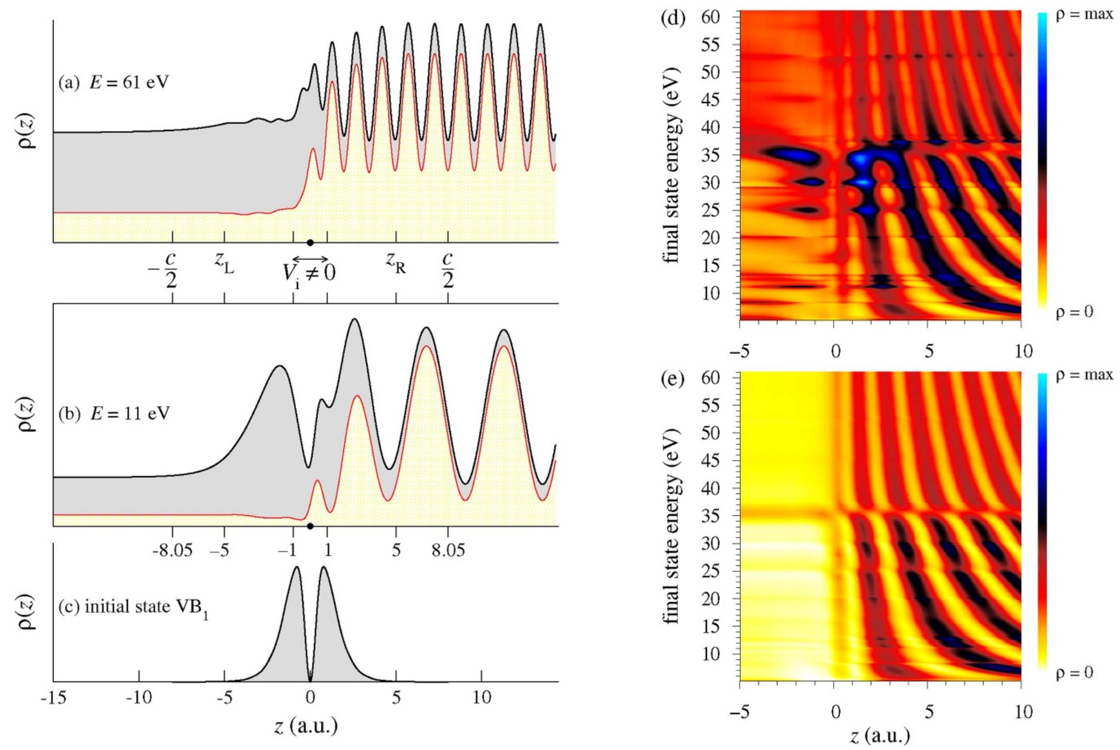

Figure 1. (a) and (b) Probability density profile $\rho(z)$ of the normal incidence LEED state for $E - E_{\mathrm{VBM}} = 61$ eV (a) and 11 eV (b). The 7-AGNR plane is at $z = 0$. Thick black line is the total density and thin red line (yellow shaded area) is the $\mathbf{G}_{||} = 0$ contribution $|\phi_{\mathbf{G}_{||}=0}(z)|^2$, see equation (3). The gray shaded area shows the contribution from the $\mathbf{G}_{||} \neq 0$ surface Fourier harmonics. The artificial supercell, see section 5, extends from $-c/2$ to $c/2$. (c) Density profile of the VB_1 initial state. (d) Energy-depth distribution $\rho(z,E)$ of the LEED state density. (e) $\mathbf{G}_{||} = 0$ contribution to $\rho(z,E)$.

augmented plane waves (APWs) using the variational embedding method of [25], see section 5. The right vacuum half-space $z > z_{\mathrm{R}}$ contains the incident wave and reflected waves. Then the Laue representation of the LEED state reads

$$\Phi_{\mathrm{LEED}}\left(\mathbf{r}_{||}, z\right) = \sum_{\mathbf{G}_{||}} \phi_{\mathbf{G}_{||}}(z) \exp\left[i\left(\mathbf{k}_{||} + \mathbf{G}_{||}\right)\mathbf{r}_{||}\right], \tag{2}$$

where $\mathbf{r}_{||}$ is the position vector parallel to the 7-AGNR plane and $\mathbf{G}_{||}$ are reciprocal lattice vectors.

An example of the scattering solution for the normal emission at two energies $E = 61$ and 11 eV relative to the valence band maximum (VBM) is presented in figures 1(a) and (b) as the density profile of these LEED states

$$\rho(z) = \int |\Phi_{\mathrm{LEED}}\left(\mathbf{r}_{||}, z\right)|^2 \, \mathrm{d}\mathbf{r}_{||}. \tag{3}$$

Note that in the interior of the nanoribbon the contribution from the Fourier harmonics with reciprocal lattice vectors $\mathbf{G}_{||} \neq 0$ (gray) strongly exceeds the $\mathbf{G}_{||} = 0$ contribution (yellow) both at low and at high energies, and the $\mathbf{G}_{||} \neq 0$ contribution does not decrease with energy. This makes a free-electron approximation for the final state highly questionable [26] in this energy range.

2.2. Photon energy and polarization dependence of photoemission from GNRs

In our experiment the bisector plane (set by the light incidence direction and the analyzer central axis) is perpendicular to the GNR long axis, figure 2(a), the latter being parallel to the analyzer entrance slit (see section 4 for experimental details). The ribbons align parallel to the steps (in the $[1\bar{1}0]$ direction of the substrate), as established for the Au(788) surface at the atomic and mesoscopic scale by LEED and scanning tunneling microscopy (STM) in [18, 27, 28].

Figure 2(b) shows the VB_1 dispersion of 7-AGNRs along the ribbon (i.e. in the ΓM direction of the hexagonal Brillouin zone (BZ) of graphene) measured with a p-polarized light of $\hbar\omega = 13$ eV in the experimental geometry of Figure 2(a). The band maximum is at Γ and has a binding energy of $E_{\mathrm{VB}_1} = 0.86$ eV, which agrees with the previous results [18, 19]. Above this band the surface state of the Au(788) substrate can be identified, indicating an excellent surface quality coexisting with the GNR formation.

Figure 2(c) presents the photon energy dependence of the normal emission from VB_1 for the p-polarized light from 12 to 40 eV in steps of 1 eV. We find a strong photoemission intensity modulation

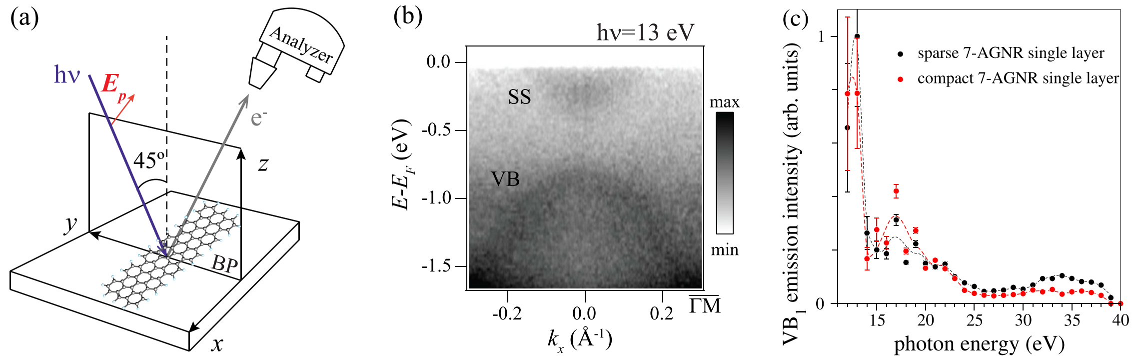

Figure 2. (a) ARPES experimental setup. The bisector plane (BP) is spanned by the light incidence direction and the central angle of the analyzer. For *p*-polarization the electric field of the light **E** lies in this plane, and for *s*-polarization it is perpendicular to the BP. The analyzer slit is aligned along the *x*-axis, i.e. perpendicular to the BP. (b) ARPES scan of 7-AGNRs on Au(788) along the ΓM direction in the first 7-AGNRs BZ with a *p*-polarized light of $\hbar\omega = 13$ eV. The surface state of Au(788) dispersing towards Fermi energy and the oppositely dispersing VB_1 of the GNRs are clearly visible. (c) Photon energy dependence of the intensity of the VB_1 at Γ in this experimental geometry. Two measurements of different samples are shown: black circles are for a sparse 7-AGNR layer coverage, while red ones are for a compact GNR monolayer completely covering the surface. In both cases the intensity peaks at 12 and 13 eV and almost vanishes above 39 eV. The dashed lines are guides for the eye.

characterized by a dominant peak at the lowest photon energies (12 and 13 eV), an attenuation up to 25 eV, and intensity depletion of the band above 39 eV. Above this energy and up to 95 eV, the normal emission from VB_1 cannot be discerned from the background, see figure S1 in supplementary information. This explains why the band at Γ was practically undetectable in previous ARPES experiments with photon energy above 32 eV [19, 28–30]. Interestingly, such enhanced low energy photoemission does not occur in suspended graphene, which exhibits the strongest emission at 37 eV according to our previous calculations [31]. Such conspicuous differences warrant investigation of the origin of the different photoemission signals from AGNRs, for which an *ab initio* one-step theory is instrumental.

As illustrated by the density distribution in figure 1(d), the LEED wave function may rapidly change with energy manifesting sharp resonances (e.g. at 11 eV, see figure 1(b)). Note that the rapid energy variations are mainly due to the $\mathbf{G}_{||} \neq 0$ surface harmonics. Still, the $\mathbf{G}_{||} = 0$ map (figure 1(e)) exhibits a conspicuous feature at 36 eV, which apparently is a manifestation of the scattering resonance due to the coupling of the in-plane and perpendicular motions, characteristic of the graphene monolayer (see also figure 5(d) and a detailed analysis in [32]).

One would expect such rapid variations of the photoelectron final state to give rise to an appreciable photon energy dependence of photoemission. Therefore, we study the top of the valence band of the nanoribbon, which is known to be formed by three hole bands: VB_1, VB_2, and VB_3 [19] (see figure 3(a)). The planar density distributions for the three states at Γ are shown in figures 3(b)–(d). The analysis of the wave functions (not shown) suggests that the VB_1 state is even on reflections in both *x* and *y* directions, while VB_2 is odd in both reflections and VB_3 is odd on the $x \to -x$ and even on the $y \to -y$ operation. This is illustrated by the nodal lines seen as horizontal and vertical white voids in the $\rho(\mathbf{r}_{||})$ maps in figures 3(c) and (d). Thus, the only Cartesian component of the momentum operator that contributes to the dipole transition from the VB_1 state is p_z, and for VB_3 it is p_x. In contrast, the dipole photoemission from VB_2 at $k_x = 0$ vanishes.

The above analysis suggests that VB_1 should be visible in *p*-polarized light because it is even under reflection in the scattering plane. This is easily verifiable because different light polarizations can be realized by simply rotating the sample around the *z* axis, see figure 4, and switching between *s*- and *p*-polarization. Figures 4(a) and (b) summarize the four geometries for $\hbar\omega = 21$ eV. The grayscale maps show the photoemission intensity as the isoenergetic cut at -0.8 eV (upper graphs, figures 4(c) and (d)), the energy-momentum intensity distributions along the ribbon (middle graphs, figures 4(e) and (f)), and perpendicular to the ribbon (lower graphs, figures 4(g) and (h)).

As can be expected from the symmetry of the initial states, figure 3, regardless of the GNR orientation the *s*-polarization suppresses the emission from VB_1 state. In contrast, the *p*-polarization allows the normal emission from the VB_1 band due to the $\mathbf{E} \parallel \mathbf{z}$ component of the incident light. (The VB_1 state is odd in $z \to -z$ reflection, but this does not lead to a symmetry selection rule because Φ^*_{LEED} is not symmetric under the reflection $z \to -z$, see figure 1.) Two related observations can be made: on the one hand, the VB_1 state is practically invisible for the *s*-polarization with the incidence plane parallel to the ribbon, geometry in figure 4(b). On the other hand, intensity modulations clearly show up in the $I(k_y, E)$

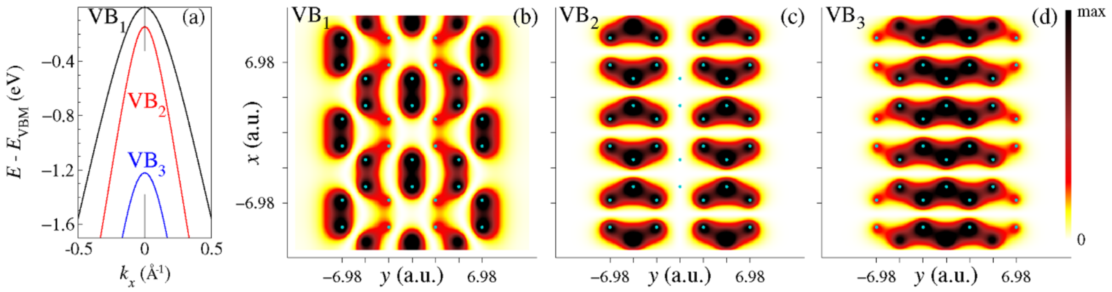

Figure 3. (a) Dispersion along the ribbon $E(k_x)$ of the valence bands VB$_1$, VB$_2$, and VB$_3$. Planar density distributions $\rho(\mathbf{r}_{||})$ at $k_x = 0$ of VB$_1$ (b), VB$_2$ (c), and VB$_3$ (d). The density is obtained with a full-potential linear APW method, see section 5.

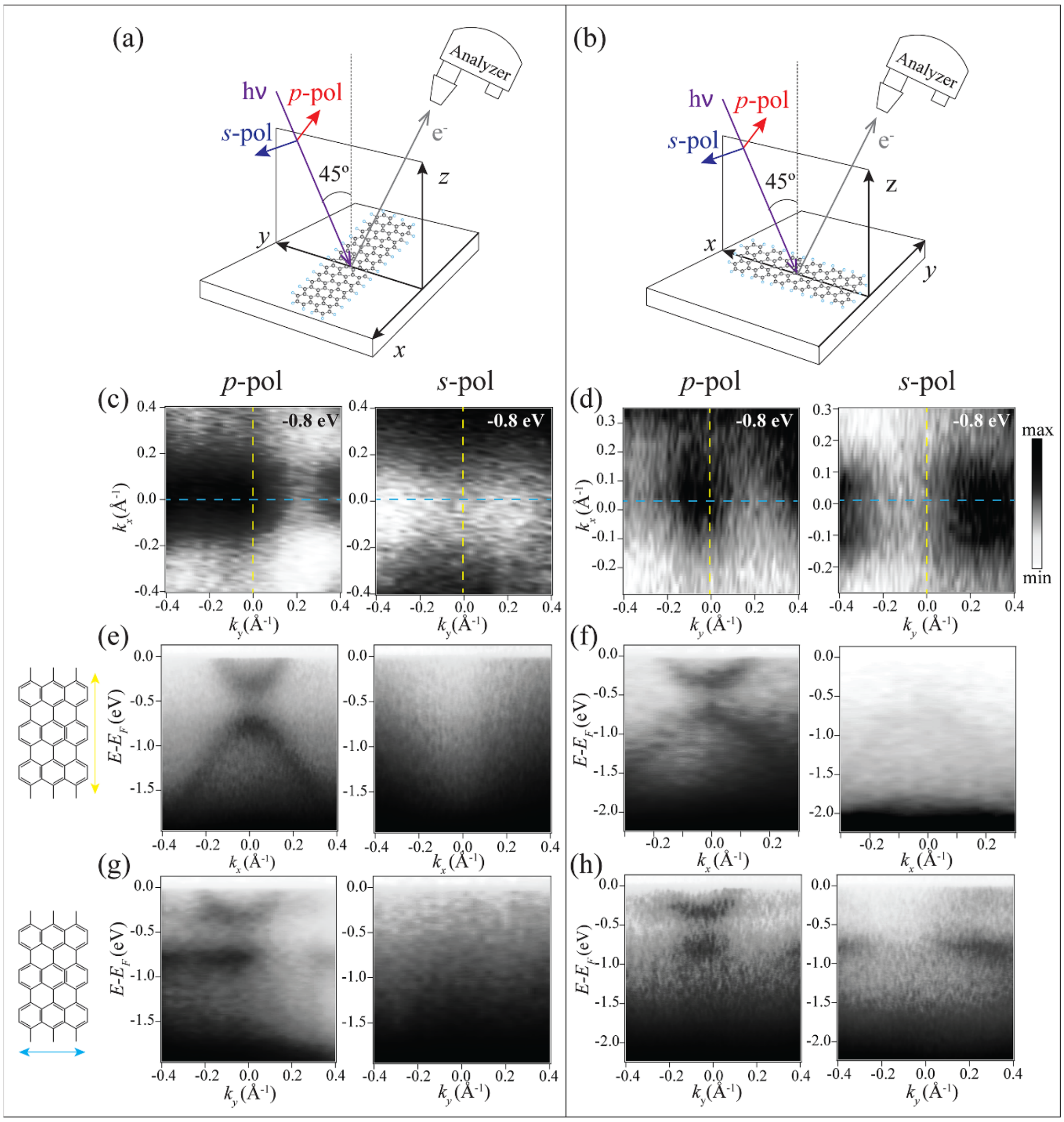

Figure 4. Four measurement geometries of the ARPES experiment on graphene nanoribbons: For two orientations of the light incidence plane, perpendicular (a) and parallel (b) to the GNR, measurements with *s* and *p*-polarized light are presented. Panels (c) and (d) show the angular distributions of the photoemission intensity at the binding energy of 0.8 eV for $\hbar\omega = 21$ eV for *yz* and *xz* incidence plane, respectively. Panels (e) and (f) show the energy-momentum intensity distribution for **k** along the GNR (ΓM line of graphene), and panels (g) and (h) for **k** perpendicular to the GNR (ΓK line). The concave-up dispersion of the surface state of the Au substrate is observed in both directions, whereas VB$_1$ disperses only along the GNR. Conversely, perpendicular to the ribbon, only the VB maximum can be observed. This confirms the 1D nature of the GNRs and their alignment with the substrate steps.

maps, right graph of figure 4(h). Interestingly, the VB_1 state becomes quenched at $\hbar\omega = 21$ eV when the ribbon is perpendicular to the incidence plane (parallel to the s-polarization direction), see right graphs of figures 4(e) and (g). Note that the VB_2 state is not visible in s-polarization for both configurations in figure 4 because it is odd in both $x \to -x$ and $y \to -y$ reflections, and the time-reversed LEED state for the normal emission is even in both reflections.

Having validated the symmetry of the VB_1 state by switching the light polarization, let us theoretically investigate the photon energy dependence of the emission from Γ. Figures 5(a) and (b) show the normal emission from VB_1 for $\mathbf{E} \parallel \mathbf{z}$ and from VB_3 for $\mathbf{E} \parallel \mathbf{x}$, denoted by I_1^z and I_3^x, respectively. Both CIS spectra manifest very strong enhancement of the emission intensity in a narrow interval between 11 and 13 eV final energy, above which $I_1^z(\omega)$ rapidly drops by an order of magnitude and keeps decreasing to remain two orders of magnitude lower than the maximum over the energy range from 15 to 60 eV. Our experiment, figure 2(c), convincingly confirms the theoretical prediction and refutes the statement of [19] that VB_1 'is only visible in a narrow range of emission angles', namely at large k_y. The conclusion of [19] stemmed from the assumption of a simple quantum-well-like quantization rule for the y-dependence (perpendicular to the ribbon) of the initial state wave function together with the plane-wave assumption for the final state. In fact, the y-dependence of the VB_1 wave function cannot be reduced to a single standing wave (as illustrated in figure 3(b)), and the failure to observe VB_1 at $k_y = 0$ is explained by the specific photon energy $\hbar\omega = 45$ eV employed in [19].

Apart from the sharp peak at 12 eV, the experiment shows a broad intensity enhancement around $\hbar\omega = 17$ eV, which does not seem to have a counterpart in the calculated spectrum. Figure 2(c) suggests that the intensity of this structure relative to the main peak and to the intensity at the higher energies strongly depends on the coverage. Therefore, we speculate that this feature may be due to an interaction between the nanoribbons.

The presence of the prominent peaks at $E = 12$ eV in both VB_1 and VB_3 CIS spectra raises the question of whether their origin can be explained solely by the energy dependence of the gross features of the final states Φ^*_{LEED}. In other words, to which extent does the CIS spectrum characterize the initial state? For this purpose we compare the CIS spectra with the energy dependence of the dwell time $\tau(E)$ in figure 5(c) (the probability to find the LEED state electron in the interval between $z = -3$ and 3 a.u.) and with the electron transmission spectrum $T(E)$ (transmitted fraction of the incident flux) in figure 5(d). The quantity $\tau(E)$ is relevant because its rapid variations must be reflected in the matrix element of equation (1). The transmissivity $T(E)$ deserves attention because it can be measured in an independent LEED experiment. Figure 5, however, illustrates that the dominant peak has a rather subtle origin: it is evident that while $\tau(E)$ has a prominent structure in this region, the other sharp maxima of $\tau(E)$ do not correspond to photoemission enhancement. Also the transmission spectrum, figure 5(d), does not show any signature of the sharp intensity enhancement. This means that a detailed knowledge of the final state wave function $\Phi^*_{\mathrm{LEED}}(\mathbf{r})$ is required to predict the intensity enhancement and that simplified approaches to photoemission should be used with care.

Nevertheless, it is instructive to compare the $T(E)$ spectra of the nanoribbon grating and of the perfect graphene layer [32], see figure 5(d). On a large scale the two spectra have similar shape with a characteristic maximum just above the resonance due to the quasi-stationary state first reported in [32]. The presence of the armchair edges does not destroy the resonance (see also figures 1(d) and (e)), but the transmission does not drop to zero below the resonance apparently because of the voids between the nanoribbons. The irregular fine structure of the nanoribbon $T(E)$ is due to the scattering induced by the edges.

2.3. Off-normal emission and the standing-wave character of the valence band states

Let us now consider the angular dependence of the photoemission from the valence bands VB_1, VB_2, and VB_3 with the wave vector of the outgoing electron having non-zero components both along (k_x) and perpendicular to (k_y) the nanoribbon. The k_y-dependence of the photocurrent $I(k_y)$ is expected to reflect the confined character of the initial states. It was thoroughly studied experimentally in [19], who observed a sharp increase of the photocurrent at specific k_y. The authors interpreted the $I(k_y)$ peaks in terms of a tight-binding model with hard-wall boundary condition [33]. According to this model, for the 7-AGNR the coefficients c_n of the orbitals in the nth atomic row ($n = 1, 2, \ldots, 7$) obey the condition $c_n = \sin(pn\pi/8)$, which corresponds to standing-wave quantized wave vectors $q_p = p\pi/4a\sqrt{3} = p\Delta$ with $\Delta = 0.32\,\text{Å}^{-1}$. The valence bands were identified as $p = 5$, 6, and 7 for VB_1, VB_2, and VB_3, respectively. The planar density distributions in figure 3 are in perfect accord with this assignment. It was assumed in [19] that the intensity enhancement occurs when k_y is close to q_p. As we will show below, the one-step theory suggests a more complicated picture.

Figure 6 shows our *ab initio* one-step calculations of the four constant k_y scans $I(E, k_x)$ measured in [19] with a photon energy of $\hbar\omega = 45$ eV. We consider only the case $\mathbf{E} \parallel \mathbf{z}$ because the in-plane contributions E_x and E_y are much smaller. The theory agrees well

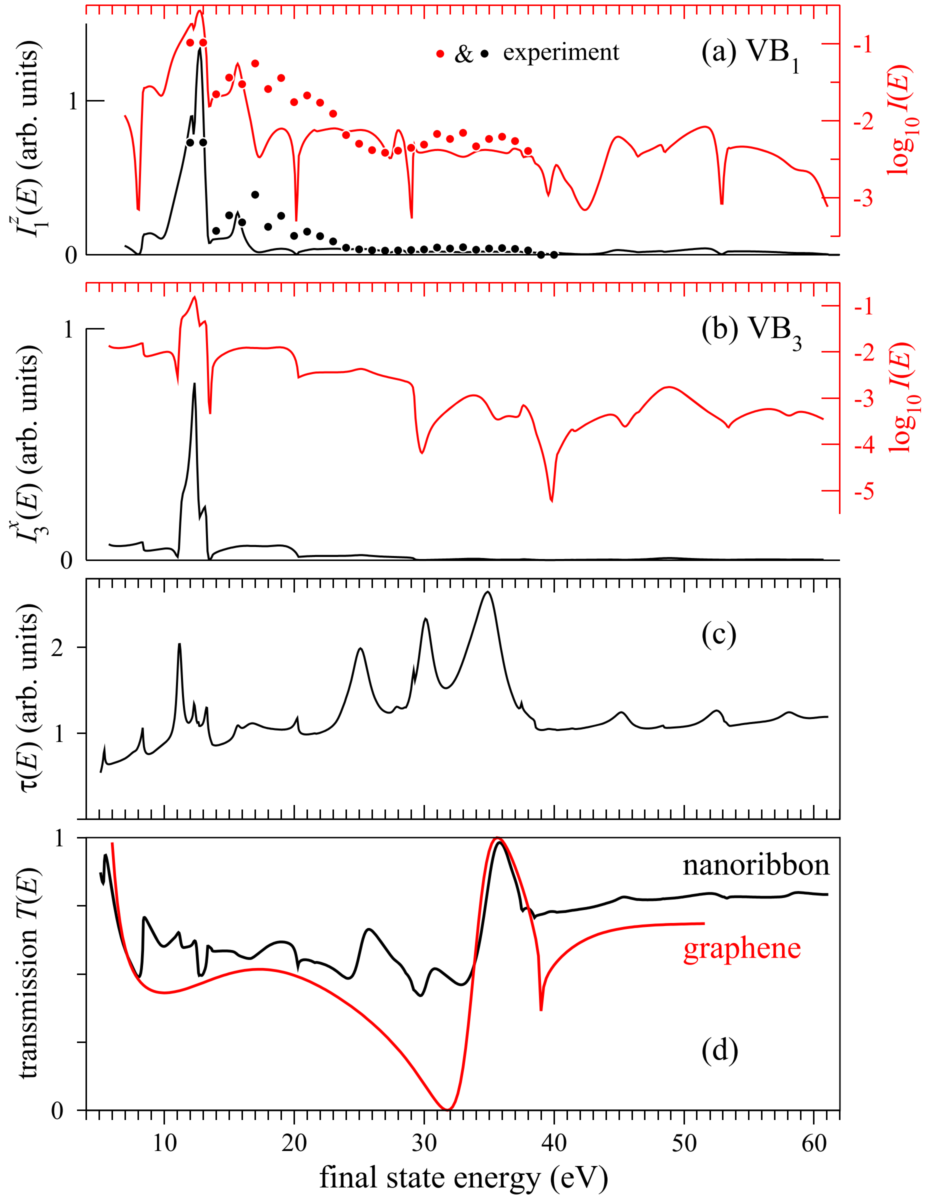

Figure 5. Photocurrent from the VB$_1$ state for **E** ∥ **z** (I_1^z) (a) and of the VB$_3$ state for **E** ∥ **x** (I_3^x) (b) versus final state energy relative to the VBM. Red lines are logarithmized intensities referred to the right axes. (c) Dwell time in the interval between $z = -3$ and 3 a.u. (d) Electron transmission through the nanoribbon superstructure (black) and through the graphene layer (red). The graphene spectrum is slightly shifted in energy so that the locations of the maxima coincide. Black and red circles in graph (a) show the experimental intensity and its logarithm, respectively, for the compact 7-AGNR monolayer, see figure 2(c).

with the experiment of [19] regarding the relative intensity of VB$_1$, VB$_2$, and VB$_3$ emission for four values of k_y. At $k_y = 0$, VB$_2$ is not visible for $\mathbf{E} \parallel \mathbf{z}$ because it is odd under the reflection $y \to -y$. VB$_1$ and VB$_3$ are even, so the very weak emission from three of the four $k_y = 0$ branches is due to more subtle aspects of the initial and final states. In particular, the VB$_1$ emission is rather strong at $\hbar\omega = 12$ eV, see section 2.2. In general, the k_y-dependence of the VB$_{1-3}$ emission is rather non-trivial: only the ascending branches are visible for $k_y = 0$, 0.3, and 0.75 Å^{-1}, and only the descending branch of VB$_1$ for $k_y = 1.35$ Å^{-1}.

Having established that the one-step theory adequately describes the experimentally observed k_y-variations of the relative intensities, let us analyze in more detail the k_y-dependence of the photocurrent for $k_x = 0$ and 1.47 Å^{-1}, i.e. for the center of the 1$^{\text{st}}$ (Γ) and of the 2$^{\text{nd}}$ BZ (point M of the hexagonal BZ). The $I(k_y)$ curves for six VB states of highest emission intensity at Γ and M are shown in figure 7. For all the states the curves for $\hbar\omega = 45$ and 18 eV are rather similar (apart from very low energies the shape of the curves varies rather moderately up to $\hbar\omega = 50$ eV). The $I(k_y)$ curves exhibit significant structure for k_y much smaller than $p\Delta$ ($\Delta = 0.32$ Å^{-1}), and for

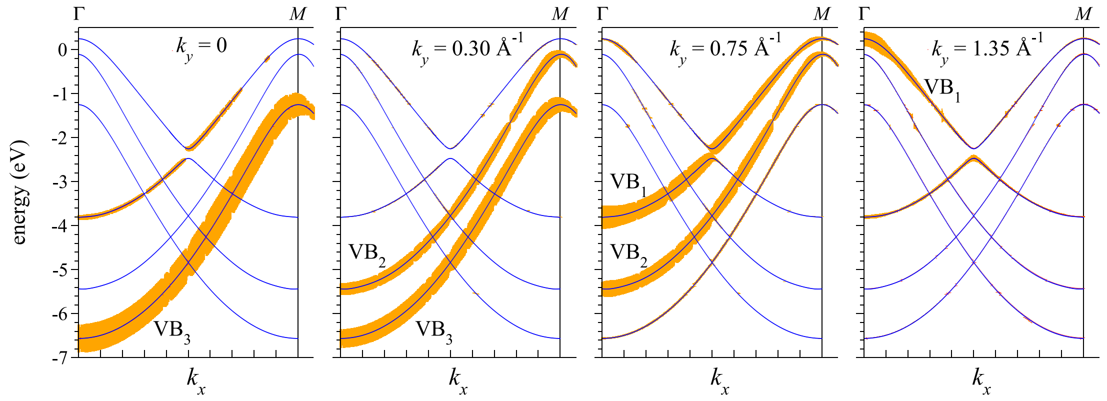

Figure 6. Energy-momentum distribution of the photocurrent $I(E,k_x)$ from VB$_1$, VB$_2$, and VB$_3$ (blue lines) for $\hbar\omega = 45$ eV for and $k_y = 0, 0.3, 0.75$, and 1.35 Å^{-1} for $\mathbf{E}||\mathbf{z}$. Photoemission intensity is proportional to the vertical extent of the shaded area.

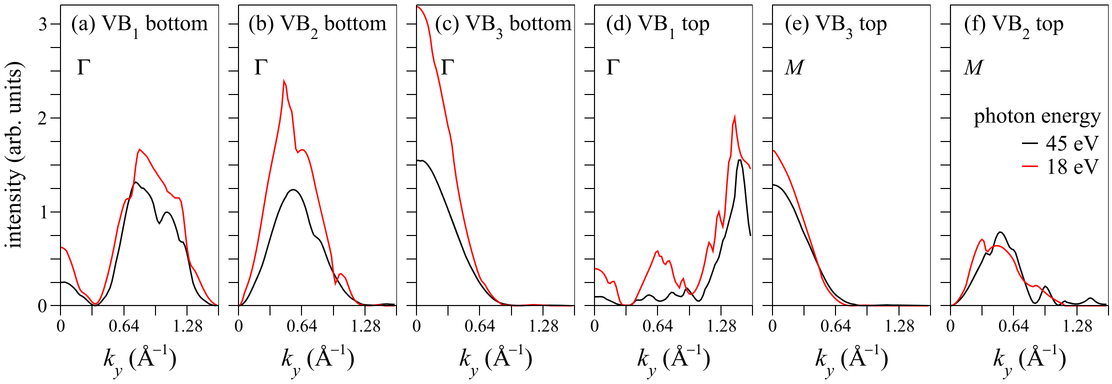

Figure 7. Photocurrent from VB$_1$, VB$_2$, and VB$_3$ at Γ (a)–(d) and at M (e) and (f) as a function of the transverse wave vector k_y for light polarization $\mathbf{E}\,||\,\mathbf{z}$ for photon energies $\hbar\omega = 45$ (black) and 18 eV (red). States of the strongest photoemission intensity are shown: at the bottom (a)–(c) and at the top (d)–(f) of the respective bands, see figure 6.

VB$_1$ ($p = 5$) the intensity decreases towards $p\Delta$. This points to the limitations of the tight-binding model of [33] in application to photoemission, and at the same time highlights the importance of the small-k_y range for the characterization of the valence band of GNRs.

3. Conclusions

To summarize, we have experimentally observed a sharp enhancement of the photoemission intensity from the VBM of the 7-AGNRs at photon energies 12–13 eV and detected significant intensity modulations depending on the polarization of the incident light, which are explained by symmetry of the initial states. The spectral narrowness of this peak and its sensitivity to the light polarization makes the 7-AGNRs interesting as vacuum ultraviolet photodetectors. These results are perfectly corroborated by the *ab initio* one-step calculation, which predicts the intensity ratio of more than an order of magnitude between $\hbar\omega = 12$ eV and $\hbar\omega > 20$ eV. The sharp peak has a rather subtle microscopic origin, in the sense that it does not have obvious counterparts in the transmission or dwell-time spectra of the final states. Nevertheless, the fact that the theory gives the correct intensity enhancement at the right energy without resorting to any adjustable parameters unambiguously points to the intrinsic nature of this feature and to its origin from the structure of the final states. A consistent discussion of the experiment is thus possible only through the eyes of the one-step photoemission theory. The adequacy of the present theory is further demonstrated by its very good agreement with the measurements of [19] for four selected values of the ribbon-transverse momentum k_y. The detailed study of the k_y-dependence of the photocurrent from the top of the valence band reveals strong intensity variations, with every band VB$_1$, VB$_2$, and VB$_3$ having a characteristic individual shape of the $I(k_y)$ curve. This analysis also reveals limitations of the tight-binding model with hard-wall boundary conditions [33] and generally of the standing-wave approach to the electronic structure of nanoribbons. Being aware of such complex angular and energy behavior of the photoemission from the GNRs is important for the ARPES studies of the electronic structure of a wide range of low-dimensional structures. Moreover, it could become key for the future development of more efficient and energetically effective ultraviolet photodetectors.

4. Experimental methods

The ARPES experiments were performed at the CASSIOPEE beamline at the SOLEIL synchrotron with the measurement geometry shown in figure 2(a). The measurements were taken using a Scienta R-4000 high-resolution (25 meV and 0.1°) hemispherical electron analyzer. The sample was kept at 100 K during ARPES measurements.

The Au(788) single crystal was prepared in UHV following standard ion sputtering and annealing cycles. The 7-AGNRs were grown on Au(788) by OSS of commercial 10,10′-dibromo-9,9′-bianthracene molecules following the recipe of [34]. This ensures that the GNRs are aligned parallel to the steps of the substrate surface, as established previously in references [18, 27, 28]. We determined the step direction from the splitting of the substrate spots in the LEED pattern. By rotating the sample around the surface normal we aligned the GNRs parallel (perpendicular) or perpendicular (parallel) to the bisector plane (analyzer slit). Prior to the ARPES experiment at the synchrotron we oriented our pristine crystal using LEED in our home laboratory and checked this at the atomic scale with STM. Then, we repositioned the sample on the sample plate so that the step direction coincided with the main axis of the sample holder with the accuracy of 5°. During the ARPES beamtime we confirmed the step geometry using the LEED optics and verified it by checking the Fermi surface maps.

Concerning the determination of the ribbons' coverage on Au(788), the growth of 7-AGNRs on Au surfaces by OSS is self-limiting to one monolayer mainly due to the necessity of catalyzing surface Au atoms to induce the Ullmann coupling of the molecular precursors used. We compared the compact single layer data measured at the synchrotron with those obtained in our home laboratory from the samples covered by one layer of 7-AGNRs grown on Au(788), where we could perform room temperature STM, ARPES (at 21 eV), LEED and XPS on the same sample. For the lower coverage sample measured at the synchrotron it is more difficult to determine the exact density of GNRs. The clear increase in the intensity of the Au surface state suggests that there is more clean surface area. Without characterization by XPS and STM, not possible at the beamline, we cannot determine the exact coverage of the sparse layer.

The ribbons' VB_1 at normal incidence was measured with p-polarized light from 12 to 95 eV in steps of 1 eV. A typical image in the long-axis direction of the GNR is shown in figure 2(b). The photon energy of 12 eV is the lowest that we could confidently access with our measurement setup, as lower energies led to strong imaging distortions. The data acquisition was repeated on different sample preparations, and similar results were obtained. For each photon energy, the photoemission spectra were normalized to the photon flux by scaling the intensity to the photocurrent measured at the last refocusing mirror. After the normalization, the normal emission energy distribution curves of the 7-AGNRs were fitted with two Gaussian peaks accounting for the Au Shockley surface state bottom and the VB_1 top convoluted with a linear background and a Fermi–Dirac distribution. The area obtained from the fit of the VB_1 peak was then plotted against the photon energy as black circles in figure 2(c), where the error bars refer to the uncertainty of the photon flux normalization (dividing the photoemission spectra by the mirror photocurrent) and the statistical error from the fitting procedure. The dashed lines in figure 2(c) are not fitted curves but are just a guide for the eye.

We intentionally used a single grating for the photon range between 12 to 40 eV to reduce possible instrumental errors, which, however, introduces a larger error at low photon energies due to the low photon flux, as plotted in figure 2(c). The uncertainty rapidly decreases above $\hbar\omega = 18$ eV due to the stabilization of the photocurrent.

The experiment definitely shows a broad enhancement of emission intensity around 17 eV (figure 2(c)), while the theory yields a weaker structure at 15 eV. This maximum is considerably less pronounced in the 'submonolayer' sample than in the densely packed one. This suggests that this feature may be due to a lateral (most probably substrate mediated) interaction between the nanoribbons: It is much weaker at the 'submonolayer' coverage because of a less regular spacing between the nanoribbons with a more significant misalignment.

5. Computational details

The scattering problem is solved with the variational embedding method of [25], which seeks the wave function Φ_{LEED} in the scattering region as a superposition of the Bloch eigenfunctions $\psi_{\lambda\mathbf{k}_{||}}$ of the auxiliary three-dimensional z-periodic crystal, which contains the scattering region as a part of the unit cell, see figure 1(a). The scattering function $\Phi^{*}_{\mathrm{LEED}}(\mathbf{r})$ is a solution of the Schrödinger equation for a true crystal potential obtained within the density functional theory (DFT), and which includes the Z/r singularity at the nucleus. The linear combinations of $\psi_{\lambda\mathbf{k}_{||}}$ is chosen so as to best satisfy the Schrödinger equation in the scattering region and to match at the planes z_{L} and z_{R} the function and derivative of the plane-wave representations in the vacuum half-spaces. The scattering basis set comprised 900 ψ functions with energies up to about 90 eV above the VBM. The Laue representation (2) was obtained by a straightforward expansion of the all-electron wave function in terms of 17 995 plane waves, $G < 7.1\,\text{a.u.}^{-1}$, and it comprised 181 surface reciprocal vectors, $G_{\|} < 3.5\,\text{a.u.}^{-1}$. The supercell lattice constants are $c = 16.11$ a.u. perpendicular to the graphene plane and $a = 23.253$ a.u. perpendicular to the ribbons. The potential of the auxiliary crystal is determined self-consistently within the local density approximation of the DFT by the full-potential APW-based augmented Fourier components method [35]. The wave functions of the initial states and the ground-state density distributions in figure 3 are obtained with this method.

Data availability statement

All data that support the findings of this study are included within the article (and any supplementary files).

Acknowledgment

I P-Z acknowledges support from Prof. Johannes V Barth (TUM). We acknowledge financial support from the Spanish Ministry of Science and Innovation (MCIN, Grants No. PID2019-107338RB-C63, PID2019-107338RB-C64 & PID2019-105488GB-I00 / AEI / 10.13039/501100011033 and RED2018-102833-T), from the Basque Government (IT1591-22), and from the regional Governments of Aragon (E12-20R). The research leading to this result has been supported by the project CALIPSOplus under Grant Agreement 730872 from the EU Framework Program for Research and Innovation HORIZON 2020. We acknowledge SOLEIL for provision of synchrotron radiation facilities and we would like to thank the beamline staff for assistance in using beamline CASSIOPEE.

ORCID iDs

Martina Corso https://orcid.org/0000-0002-8592-1284
Jorge Lobo-Checa https://orcid.org/0000-0003-2698-2543
Andrew P Weber https://orcid.org/0000-0002-7636-2572
Ignacio Piquero-Zulaica https://orcid.org/0000-0002-4296-0961
Zakaria M Abd El-Fattah https://orcid.org/0000-0003-2385-7704
J Enrique Ortega https://orcid.org/0000-0002-6643-806X
Eugene Krasovskii https://orcid.org/0000-0003-4246-2986

References

[1] Zheng W, Jia L and Huang F 2020 Vacuum-ultraviolet photon detections *iScience* **23** 101145
[2] Cai Q, You H, Guo H, Wang J, Liu B, Xie Z, Chen D, Lu H, Zheng Y and Zhang R 2021 Progress on AlGaN-based solar-blind ultraviolet photodetectors and focal plane arrays *Light Sci. Appl.* **10** 94
[3] Schühle U and Hochedez J F 2013 *Solar-Blind UV Detectors Based on Wide Band gap Semiconductors* (Springer) pp 467–77
[4] Qiu Q and Huang Z 2021 Photodetectors of 2d materials from ultraviolet to terahertz waves *Adv. Mater.* **33** 2008126
[5] Wang J, Han J, Chen X and Wang X 2019 Design strategies for two-dimensional material photodetectors to enhance device performance *InfoMat* **1** 33–53
[6] Clair S and de Oteyza D G 2019 Controlling a chemical coupling reaction on a surface: tools and strategies for on-surface synthesis *Chem. Rev.* **119** 4717–76
[7] Talirz L, Ruffieux P and Fasel R 2016 On-surface synthesis of atomically precise graphene nanoribbons *Adv. Mater.* **28** 6222–31
[8] Corso M, Carbonell-Sanromà E and de Oteyza D G 2018 Bottom-up fabrication of atomically precise graphene nanoribbons *On-Surface Synthesis II* ed D G, de Oteyza and C Rogero (Springer) pp 113–52
[9] Chen Z, Narita A and Müllen K 2020 Graphene nanoribbons: on-surface synthesis and integration into electronic devices *Adv. Mater.* **32** 2001893
[10] Saraswat V, Jacobberger R M and Arnold M S 2021 Materials science challenges to graphene nanoribbon electronics *ACS Nano* **15** 3674–708
[11] Liu Z, Fu S, Liu X, Narita A, Samorì P, Bonn M and Wang H I 2022 Small size, big impact: recent progress in bottom-up synthesized nanographenes for optoelectronic and energy applications *Adv. Sci.* **9** 2106055
[12] Rizzo D, Veber G, Cao T, Bronner C, Chen T, Zhao F, Rodriguez H, Louie S, Crommie M and Fischer F 2018 Topological band engineering of graphene nanoribbons *Nature* **560** 204–8
[13] Gröning O *et al* 2018 Engineering of robust topological quantum phases in graphene nanoribbons *Nature* **560** 209–13
[14] Li J, Sanz S, Merino-Díez N, Vilas-Varela M, Garcia-Lekue A, Corso M, Oteyza D, Frederiksen T, Peña D and Pascual J 2021 Topological phase transition in chiral graphene nanoribbons: from edge bands to end states *Nat. Commun.* **12** 5538
[15] Song S, Su J, Telychko M, Li J, Li G, Li Y, Su C, Wu J and Lu J 2021 On-surface synthesis of graphene nanostructures with π-magnetism *Chem. Soc. Rev.* **50** 3238–62
[16] de Oteyza D G and Frederiksen T 2022 Carbon-based nanostructures as a versatile platform for tunable π-magnetism *J. Phys.: Condens. Matter* **34** 443001
[17] Alavi S K, Senkovskiy B V, Hertel D, Haberer D, Ando Y, Meerholz K, Fischer F R, Grüneis A and Lindfors K 2020 Photodetection using atomically precise graphene nanoribbons *ACS Appl. Nano Mater.* **3** 8343–51
[18] El-Sayed A *et al* 2020 Synthesis of graphene nanoribbons on a kinked au surface: revealing the frontier valence band at the Brillouin zone center *J. Phys. Chem.* C **124** 15474–80
[19] Senkovskiy B V, Usachov D Y, Fedorov A V, Haberer D, Ehlen N, Fischer F R and Grüneis A 2018 Finding the hidden valence band of n = 7 armchair graphene nanoribbons with angle-resolved photoemission spectroscopy *2D Mater.* **5** 035007
[20] Adawi I 1964 Theory of the surface photoelectric effect for one and two photons *Phys. Rev.* **134** A788–98
[21] Mahan G D 1970 Theory of photoemission in simple metals *Phys. Rev.* B **2** 4334–50
[22] Caroli C, Lederer-Rozenblatt D, Roulet B and Saint-James D 1973 Inelastic effects in photoemission: microscopic

formulation and qualitative discussion *Phys. Rev.* B **8** 4552–69

[23] Feibelman P J and Eastman D E 1974 Photoemission spectroscopy – correspondence between quantum theory and experimental phenomenology *Phys. Rev.* B **10** 4932–47

[24] Pendry J B 1976 Theory of photoemission *Surf. Sci.* **57** 679–705

[25] Krasovskii E E 2004 Augmented-plane-wave approach to scattering of Bloch electrons by an interface *Phys. Rev.* B **70** 245322

[26] Krasovskii E E 2020 Character of the outgoing wave in soft x-ray photoemission *Phys. Rev.* B **102** 245139

[27] Linden S *et al* 2012 Electronic structure of spatially aligned graphene nanoribbons on au(788) *Phys. Rev. Lett.* **108** 216801

[28] Ruffieux P *et al* 2012 Electronic structure of atomically precise graphene nanoribbons *ACS Nano* **6** 6930–5

[29] Simonov K A, Vinogradov N A, Vinogradov A S, Generalov A V, Svirskiy G I, Cafolla A A, Mårtensson N and Preobrajenski A B 2016 Effect of electron injection in copper-contacted graphene nanoribbons *Nano Res.* **9** 2735–46

[30] Senkovskiy B V *et al* 2017 Spectroscopic characterization of N= 9 armchair graphene nanoribbons *Phys. Status Solidi* **11** 1700157

[31] Krasovskii E 2021 *Ab initio* theory of photoemission from graphene *Nanomaterials* **11** 1212

[32] Nazarov V U, Krasovskii E E and Silkin V M 2013 Scattering resonances in two-dimensional crystals with application to graphene *Phys. Rev.* B **87** 041405

[33] Zheng H, Wang Z F, Luo T, Shi Q W and Chen J 2007 Analytical study of electronic structure in armchair graphene nanoribbons *Phys. Rev.* B **75** 165414

[34] Cai J *et al* 2010 Atomically precise bottom-up fabrication of graphene nanoribbons *Nature* **466** 470–3

[35] Krasovskii E E, Starrost F and Schattke W 1999 Augmented Fourier components method for constructing the crystal potential in self-consistent band-structure calculations *Phys. Rev.* B **59** 10504–11